Evidence that the liquid structure affects the nucleation of the primary metastable L12-Al3Zr in additive manufacturing

Maxence Buttard, Guilhem Martin, Patrick Harrison, Edgar F Rauch, Béchir Chéhab, Philippe Jarry, Jean-Jacques Blandin, Patricia Donnadieu

Evidence that the liquid structure affects the nucleation of the primary metastable $L1_2$-Al_3Zr in additive manufacturing

Maxence Buttard[1], Guilhem Martin[1*], Patrick Harrison[1], Edgar F. Rauch[1], Béchir Chéhab[2], Philippe Jarry[2], Jean-Jacques Blandin[1], Patricia Donnadieu[1]

1. Univ. Grenoble Alpes, CNRS, Grenoble INP, SIMAP, F-38000 Grenoble

2. Constellium Technology Center, Parc économique Centr'Alp, 725, rue Aristide-Bergès, CS 10027, 38341 Voreppe cedex, France

* guilhem.martin@simap.grenoble-inp.fr

Abstract

The strategy aiming at promoting the precipitation of the primary metastable $L1_2$-Al_3X phase is the most widely used to refine grain size in Al alloys designed for additive manufacturing. It is generally admitted that Al grains nucleate onto the primary $L1_2$-Al_3X precipitates by epitaxy resulting in a cube-cube orientation relationship. Here we report TEM observations showing clusters of precipitates of this primary $L1_2$-Al_3X phase. Using Automated Crystallographic Orientation Mapping in the TEM, we show that such clusters consist of various orientations. Analysis of those clusters reveals that some orientations share common 5-fold rotational symmetry axes suggesting that they have nucleated from an icosahedral template. We conclude that Icosahedral Short Range Order (ISRO) in the liquid can play a role in the nucleation of the primary metastable $L1_2$-Al_3Zr phase through the ISRO-mediated nucleation mechanism.

Keywords: Additive Manufacturing; Nucleation; Al alloys; ISRO; Primary phase

During the last decade, the development of new Aluminium alloys dedicated to Laser Powder Bed Fusion (L-PBF) has largely increased for serving the growing demand for complex parts with high mechanical strength at both room and high temperature, see e.g. [1]–[3]. Unfortunately, precipitation-strengthened alloys such as the 2XXX [4], [5], 6XXX [6], [7], or 7XXX series [8]–[10] are subject to severe hot cracking issues when processed by L-PBF. To solve this issue, several strategies have been considered.

The most efficient strategy to mitigate hot cracking consists in refining the grain size. Grain refinement is usually achieved by promoting heterogeneous nucleation of the FCC-Al matrix. Introducing directly solutes such as X = Zr, Sc, and Ti in the pre-alloyed powders to promote the precipitation of the primary $L1_2$-Al_3X phase in the liquid is certainly the most promising route as shown in e.g. [4], [11]–[14] [23] [24]. Zirconium is frequently preferred to Sc or Ti for cost-efficiency [4] [7]. The benefit of using Zirconium as an alloying element in Al alloys designed for L-PBF is twofold. First, it improves their processability thanks to the grain refinement induced by the precipitation of the primary metastable $L1_2$-Al_3Zr phase [4] [25] [26]. Besides, it can be utilized to enhance the mechanical properties through a Hall-Petch effect [2], [17], [18]. It can also be exploited to harden the material through precipitation strengthening after a post-fabrication heat treatment if enough Zr is retained in solid solution during L-PBF [18]. Indeed, the formation of secondary $L1_2$-Al_3Zr nanoprecipitates is very efficient to increase the yield strength. In the presence of Zr addition, the melt pool consists of fine equiaxed grains along the melt pool boundaries (FEZ: Fine Equiaxed Zone) and columnar grains growing along the thermal gradient (CZ: Columnar Zone). As explained by Griffiths in [19] and Opprecht in [20], such a duplex grain structure is closely related to the local solidification conditions at the melt pool scale [27] [28]. Indeed, the formation of the $L1_2$-Al_3Zr primary phase is intimately linked to the solid-liquid interface velocity. Along the melt pool boundary, where the solid-liquid interface velocity is the slowest, the primary $L1_2$-Al_3Zr phase can precipitate. $L1_2$-Al_3Zr precipitates enable the nucleation of aluminium grains forming the FEZ along the melt pool boundaries. However, when going towards the melt pool center, the solid-liquid interface velocity increases, thus promoting the solute trapping of Zr and consequently inhibiting the precipitation of this primary phase. In the absence of inoculating particles, columnar growth is selected.

In parallel, it was shown that Icosahedral Short Range Order (ISRO) in the liquid can be invoked to account for the grain refinement in cast products of FCC-metals, see examples in Al-based alloys [22], [23] as well as in Au-based alloys [24]. The underlying mechanism is described as ISRO-mediated nucleation. This mechanism was recently evidenced in additively manufactured FCC metals: Al alloys [25], [26] and Ni alloys [27], [28].

Here, we report TEM observations in the FEZ of an Al alloy designed for additive manufacturing (see its chemical composition in **Table 1**) that provide new insights regarding the nucleation of the primary metastable $L1_2$-Al_3Zr phase.

Al	Mn	Ni	Cu	Zr
Bal.	3.87	3.14	1.86	1.02

Table 1 : chemical compositions in %wt measured on the pre-alloyed powder batch used for this work.

Details on the L-PBF processing conditions can be found in our previous study [26]. A thorough analysis of the role of zirconium and the formation of the primary metastable $L1_2$-Al_3Zr phase has been conducted by TEM using thin foils prepared by electropolishing using a Tenupol 5 in a solution consisting of 20% nitric acid and 70% methanol at -25 °C and 15 V. Chemical analysis through energy-dispersive X-ray spectroscopy (EDS) was performed at 200 keV using a TEM FEG JEOL 2100F and a high collection angle SDD Centurio detector. The chemical analysis was coupled with ACOM (Automated Crystallographic Orientation Mapping) using the ASTAR^{TM} hardware and software. Using a parallel nano-beam, diffraction patterns with a user-defined periodicity are collected with a CDD camera allowing to map the region of interest. The acquired diffraction data are compared with simulated diffractions of candidate phases through a template matching approach. These phases are carefully chosen based on preliminary XRD analyses and ThermoCalc solidification calculations, see e.g. [29]. Finally, the candidate phase with the highest correlation index is considered to be the solution. The correlation index measures the matching quality between the experimentally recorded pattern and the theoretical template of a given phase. The reliability of the phase recognition using the ACOM tool (R) is estimated as follows: $R = 100(1-I_1/I_2)$ with I_1 and I_2 the correlation indices of the two best solutions for the selected candidate phases. More details on this TEM technique can be found in [30] [31]. In the present study, advanced post-processing options of this technique were used to improve both phase and orientation recognition. Phase and orientation maps have been processed by using multi-indexing [32] which consists in subtracting the diffraction pattern of the matrix grains before indexing via a template matching technique. This enables improvement of the quality of phase recognition for the various intermetallic phases, in particular for the primary $L1_2$-Al_3Zr phase which is the object of interest in this work.

Figure 1 (a) shows a low-magnification EBSD (Electron Back Scattered Diffraction) map revealing multiple molten pools. At the melt pool scale, two different grain morphologies are observed in agreement with the literature, see e.g. [10], [13], [33], [34]. Regions located along the melt pool boundaries (FEZ displayed in black in **Figure 1(a)** consist of submicronic (about 600 nm on average) equiaxed grains as illustrated in **Figure 1(b)** by the orientation map collected using ACOM. Within the melt pools, columnar grains can be observed (CZ in **Figure 1(a)**).

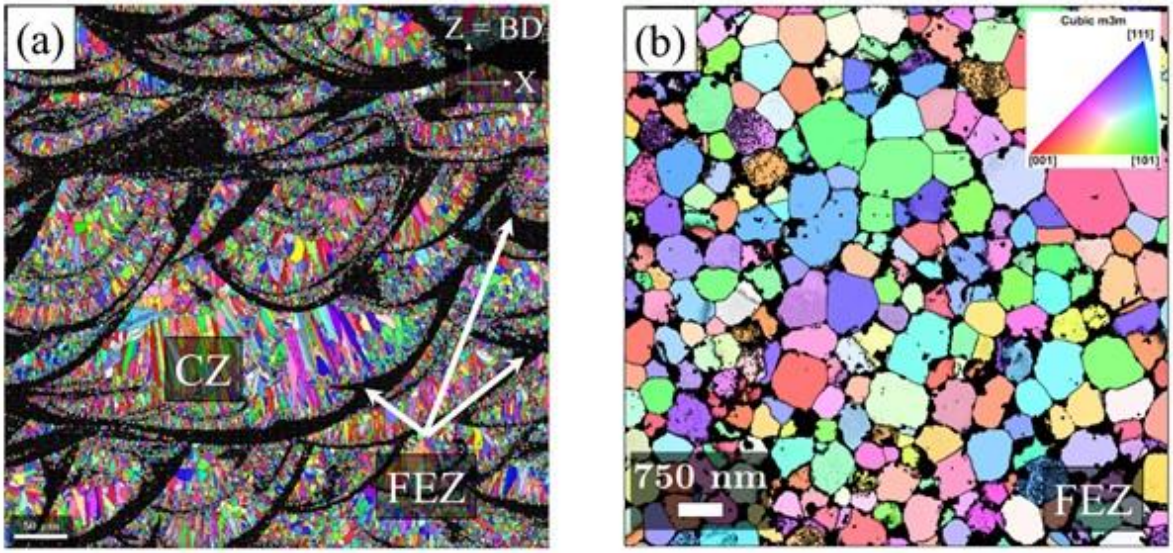

Figure 1 : (a) Low magnification IPF colour-coded EBSD map acquired using a 200 nm step size revealing various melt pools. Black regions are associated with the FEZ and could not be properly indexed using a 200 nm step size, in particular, because of the presence of a high fraction of intermetallic particles (about 35%) and small grain size (about 600 nm). (b) Example of a map collected using ACOM in a FEZ using a 15 nm step size. Here only the orientation of FCC-Al is given and black regions correspond to intermetallics.

The presence of fine equiaxed grains results from the epitaxial nucleation of the FCC phase on precipitates of the primary metastable $L1_2$-Al_3Zr phase. This mechanism is well-documented in the literature, see e.g. [16] [23] [29] [32] [34]. The present work focuses on the FEZ since the primary metastable $L1_2$-Al_3Zr phase was exclusively observed in such regions. **Figure 2(a)** shows a low-magnification TEM-BF image taken in the FEZ where intragranular precipitates can be observed. Two different morphologies of those intragranular precipitates were observed. Some intragranular precipitates show a cubic morphology (**Figure 2(b-d)**) and others exhibit a more irregular shape, see **Figure 2(e-g)**. Both morphologies are considered statistically relevant. Various intragranular precipitates showing an irregular morphology are pointed out using yellow arrows in **Figure 2(a)**. Typical regions of interest representative of those two morphologies of the intragranular precipitates have been selected and were further characterized using EDS and ACOM. Zr Elemental EDS maps shown in **Figures 2(a)** and **(e)** indicate that intragranular precipitates are Zr-rich phases. ACOM analyses were then performed in the regions of interest corresponding to the white boxes drawn respectively in **Figures 2(a)** and **(e)**. Intragranular precipitates have been identified as the metastable $L1_2$-Al_3Zr phase, see **Figures 2(d)** and **(g)**. The situation shown in **Figures 2(b-d)** corresponds to the classical mechanism often reported in the literature [16] [23] [29] [32] [34] where cubic-shaped precipitates of the metastable $L1_2$-Al_3Zr phase promote the nucleation of aluminium grains. This nucleation mechanism has its own crystallographic signature since the nucleated FCC Al grain exhibits a cube-cube orientation relationship with the cubic shape primary precipitate of the $L1_2$-Al_3Zr phase. As a result, it is usually assumed that one aluminum grain nucleates from one given cubic-shaped primary metastable $L1_2$-Al_3Zr precipitate. However, we also found more complex configurations where the primary precipitates of the $L1_2$-Al_3Zr phase show more irregular morphologies as exemplified in **Figure 2(e-g)**. These cases have been more thoroughly characterized to determine if they result from different mechanisms.

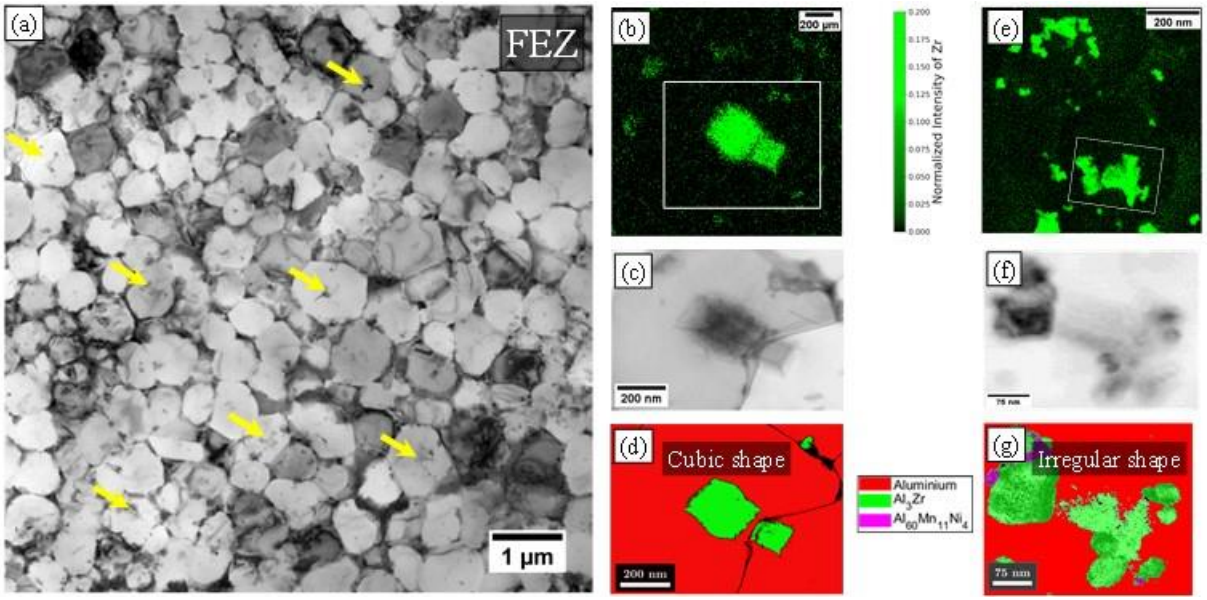

Figure 2: (a) Low-magnification TEM-BF image taken in a FEZ revealing the presence of intragranular phases based on the diffraction contrast within Al grains (see typically regions pointed out with yellow arrows). Zr elemental EDS maps, Virtual Bright Field TEM images, and phase maps determined using ACOM and showing: typical examples of (b-d) an intragranular cubic shape $L1_2$-Al_3Zr precipitate; and of (e-g) an intragranular precipitate showing an irregular morphology.

To study such complex intragranular precipitates, ACOM in the TEM turns out to be the relevant tool because one can investigate if those irregular precipitates consist of one or several crystallographic orientations. Besides, ACOM is also helpful to identify crystallographic relationships between the precipitates and the matrix or between the precipitates themselves.

The first example selected corresponds to a particle of $L1_2$-Al_3Zr showing a "sand rose" morphology as illustrated based on the phase map shown in **Figure 3(a)**. The two orientation maps corresponding to the same region of interest are given respectively in **Figure 3(b)** and **Figure 3(c)**. Those maps show that this particle with a sand-rose morphology is actually a cluster consisting of different orientations of the $L1_2$-Al_3Zr phase. The orientation labelled 9 leads to the nucleation of the Al grain labelled Grain A. The cube-cube orientation relationship between the $L1_2$-Al_3Zr orientation labelled 9 and the Grain A can be verified here thanks to the IPF colour code. Interestingly, Σ3 twin boundary orientation relationships were found between different orientations of the $L1_2$-Al_3Zr within this cluster, orientation 3 and 9 as well as orientation 6 and 7 as shown by the stereographic projection in **Figure 3(d)**. The presence of Σ3 twin relationship between orientations of this cluster is not expected for a $L1_2$ structure and can be seen as a signature of the mechanism responsible for the formation of such a sand-rose morphology. The underlying mechanism will be further discussed after having examined a second illustrative example (**Figure 4**).

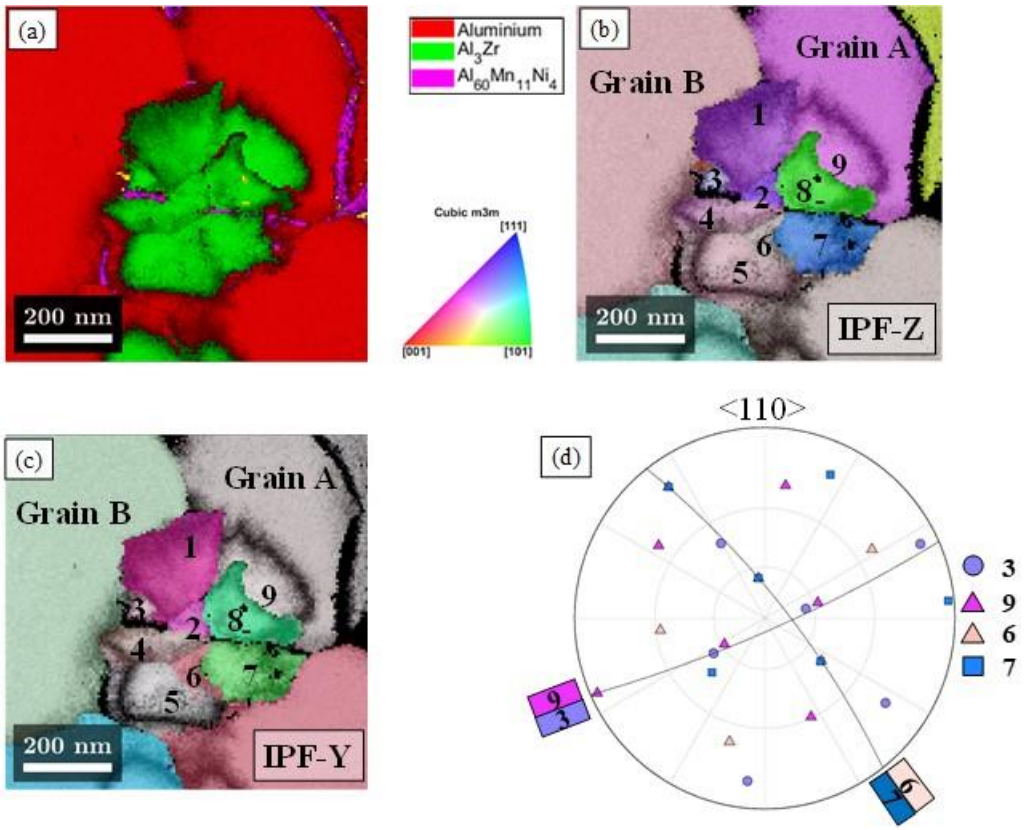

Figure 3.(a) Superimposition of the phase reliability index with the phase map revealing a sand-rose morphology for the primary metastable $L1_2$-Al_3Zr phase. (b-c) Orientation map with IPF colour coding for X and Y viewing axis showing that this particle consists of several $L1_2$-Al_3Zr phase precipitates of different orientations and cube/cube orientation with neighbouring grains. (c) Stereographic projection proving that the orientations labelled 2 and 3 are in a Σ3 twin relationship.

The second example examined in this work corresponds to the precipitate of the $L1_2$-Al_3Zr phase having an irregular morphology shown in **Figure 2(e-g)**. Once again, the ACOM analysis reveals that this irregular $L1_2$-Al_3Zr precipitate (**Figures 4(a)** and **(d)**) consists of multiple orientations, see **Figures 4(b-c)** and **(e-f)**. As many as 8 different orientations of the $L1_2$-Al_3Zr phase are found in the aluminum grain labelled Grain 1. Only one of those orientations shows a cube-cube orientation relationship with the matrix, the one labelled A in **Figures 4(b-c)** and **(e-f)**. It means that only orientation A is responsible for the nucleation of the Al grain labelled Grain 1 in **Figure 4(b-c)**. The other orientations did not generate aluminium grains, most likely because the growth rate of Grain 1 was extremely high.

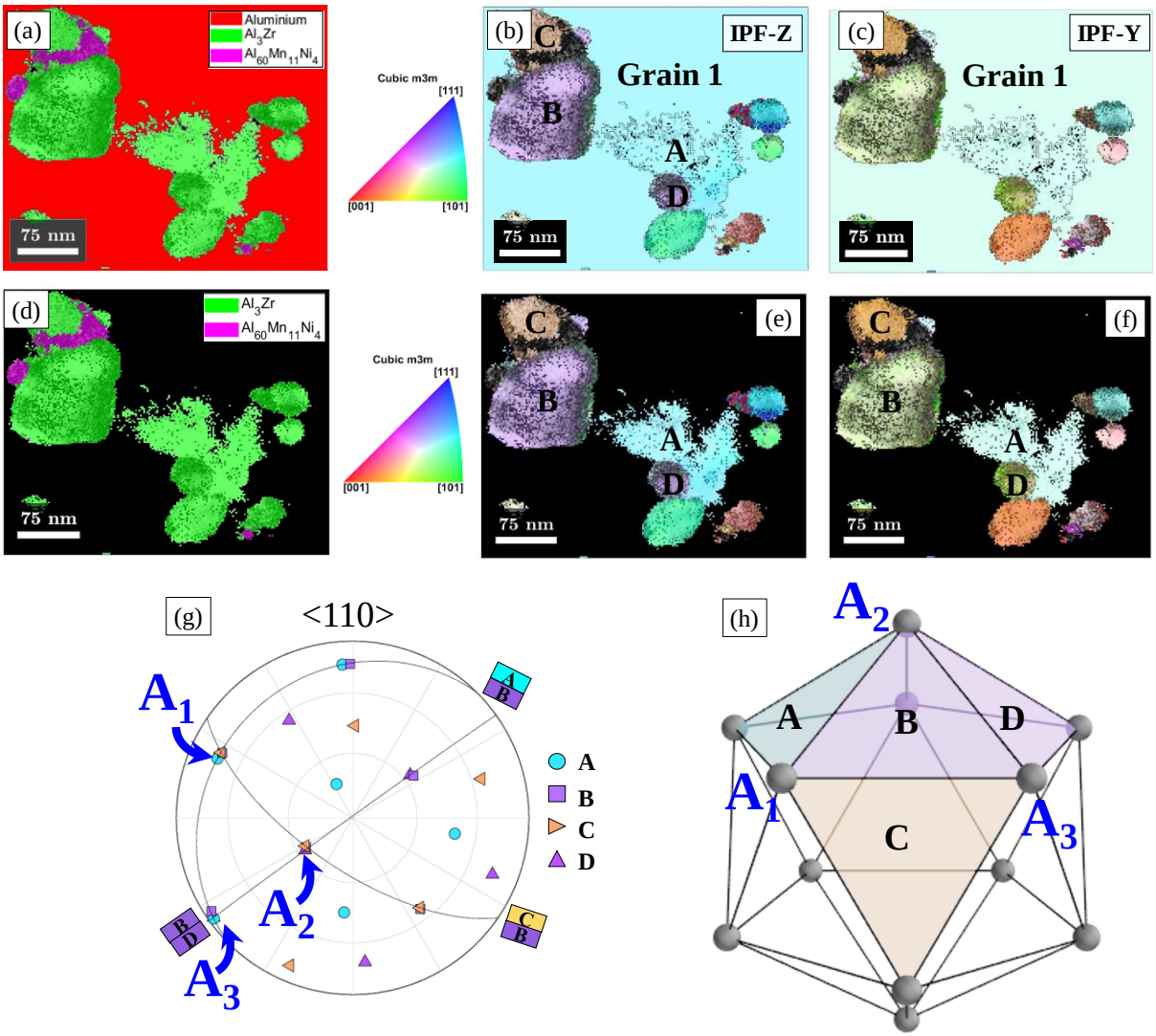

*Figure 4: Local crystallographic analysis in the region of interest highlighted using the white box in **Figure 2(e)**. (a) Phase map revealing the peculiar morphology of the $L1_2$-Al_3Zr primary phase located within an aluminium grain. Orientation maps normal to (b) the z-direction, and (c) the y-direction showing that only one of the eight orientations has the same orientation as the matrix (orientation A). (d) Phase map and orientation maps normal to (e) the z-direction, and (f) the y-direction after having removed the diffraction signal from the aluminium grain labelled Grain 1. They reveal several orientations of the $L1_2$-Al_3Zr primary phase in a single Al grain. (g) Stereographic projection of <110> directions for the $L1_2$-Al_3Zr orientations labelled A, B, C and D. A_1, A_2 and A_3 correspond to <110> directions common to 2 precipitates, respectively A and C, B, and C, B and D. (h) As illustrated by the icosahedron, the relative position of the A_1, A_2, A_3 poles are consistent with the various orientations of the Al_3Zr primary phase (A, B, C, D) inherited from an ISRO-mediated nucleation mechanism.*

Interestingly, among those eight orientations, four near-neighbour orientations (A, B, C, and D) were found to be related by a Σ3 twin orientation relationship. This can be supported by the <110> stereographic projection displayed in **Figure 4(g)** with in each case an arc of circle corresponding to a common {111} plane shared by two orientations. The colour code employed in the stereographic projection is the same as the one used in the IPF-Z map shown in **Figure 4(e)**. The $L1_2$-Al_3Zr orientations labelled A and B (resp. B and D, and, B and C) show a Σ3 twin orientation relationship. A more in-depth study reveals that the orientations A, B, and C (respectively A, B, and D, and also B, C, and D) share common <110> directions labelled A_1, A_2, or A_3 in **Figure 4(g)**. Those <110> directions shared by several $L1_2$-Al_3Zr orientations are consistent with three fivefold axes since they correspond to the intersections of twin planes, see labels A_1, A_2, or A_3 in **Figure 4(g)**. This suggests that those primary phases have nucleated from a template possessing a fivefold rotational symmetry. Fivefold axes can be found in

different local tetrahedral packing. As shown by Frank and Kasper [37], there are a limited number of local tetrahedral packing characterized by their coordination polyhedra: the icosahedron Z12 and three related polyhedra called Z14, Z15, and Z16 where the number corresponds to the number of neighbours surrounding the central atom. The coordination polyhedra can be constructed using regular tetrahedrons or slightly distorted ones as illustrated in ***Figure S* 1**. Here, the orientations A, B, C, and D of the primary $L1_2$-Al_3Zr phase found in the aluminium grain labelled Grain 1 can be positioned on an icosahedral template (**Figure 4(h)**) by respecting the orientation relationships found between those near-neighbour orientations. This analysis earlier proposed in [22], [23], [25], [27] suggests that local liquid ordering not only affects the nucleation of the aluminium matrix grains as shown in [25], [26] but could also affect the nucleation of the primary metastable $L1_2$-Al_3Zr phase through an ISRO-mediated nucleation mechanism. We found no crystallographic reason explaining why such a nucleation mechanism could not be activated for the nucleation of the primary $L1_2$-Al_3Zr phase since this phase is based on an FCC lattice such as aluminium. To go a step further, we also checked if the four orientations A, B, C, and D could be positioned on other polytetrahedral configurations (Z14, Z15, or Z16, see ***Figure S* 1** for a description of those configurations). It turns out that the orientation relationships between the near-neighbour orientations A, B, C, and D could also be positioned on a Z15 template, see ***Figure S 2***. The present results do not allow us to undoubtedly adjudicate which local ordering between Z12 or Z15 is responsible for the orientation relationship linking orientations A, B, C, and D. However, we think that the hypothetical nucleus formed in the liquid might rather be a Z15 environment instead of a perfect icosahedron (Z12). Local environments with coordination numbers higher than 12 in the liquid are indeed in better agreement with a less compact local ordering involving bigger atoms such as Zirconium. Thus, ISRO-mediated nucleation could also be invoked in the presence of less closely-packed environments with coordination numbers higher than 12. Interestingly, the number of nucleated orientations created via this mechanism could vary according to the local liquid ordering (Z12, Z14, Z15, or Z16), or in other words to the various solute elements.

The example shown in **Figure 3** can now be further discussed considering that ISRO can play a role in the nucleation mechanism of the primary metastable $L1_2$-Al_3Zr phase. Both the sand-rose morphology and the Σ3 twin boundaries found between near-neighbour orientations in microstructures inherited from solidification can be seen as a sign of the ISRO-mediated nucleation mechanism. We believe that many orientations belonging to this cluster with a sand-rose morphology cannot be observed experimentally due to the difficulty of properly capturing the signal from the other underlying orientations, supposedly present in this cluster.

Interestingly, the above results have a consequence regarding grain refinement. When ISRO-mediated nucleation affects the primary $L1_2$-Al_3Zr phase, the traditional view which considers that one precipitate of this primary metastable phase leads to the nucleation of one FCC-Al grain (see the schematic in **Figure 5(a-d)**) should be reconsidered. Indeed, we have shown here that many precipitates of the primary $L1_2$-Al_3Zr phase may actually not be useful to promote the nucleation of FCC-Al grains, see the schematic in **Figure 5(e-g)**.

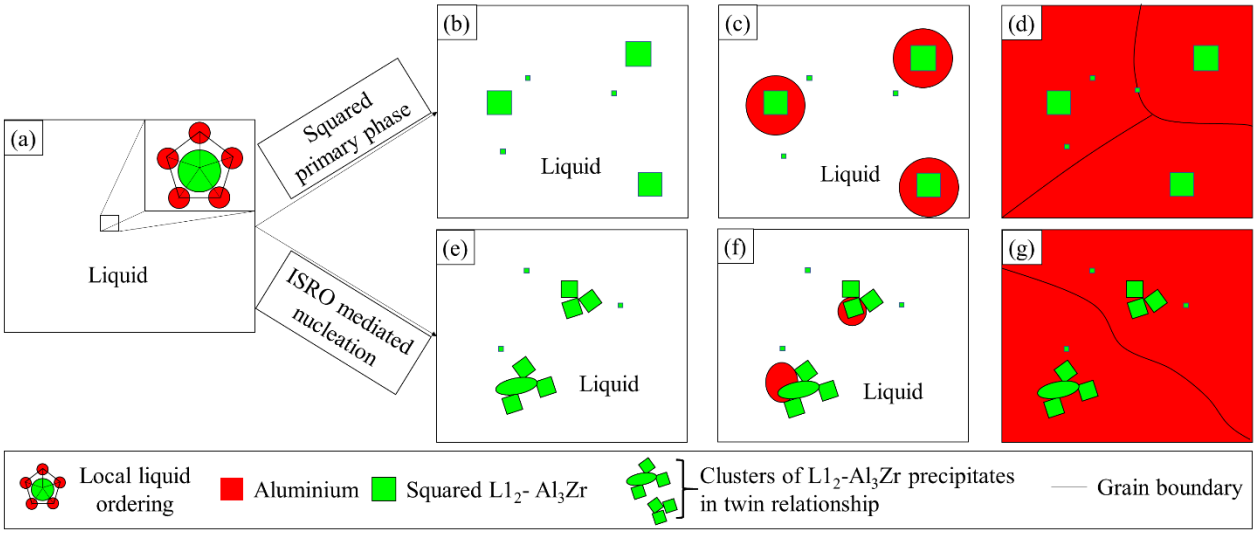

Figure 5 : Schematic representation of the two situations observed for the nucleation of the $L1_2$-Al_3Zr primary phase.

The results reported in this work give evidence that local liquid ordering might not only affect the nucleation of the FCC-matrix as already shown in [2], [13], [18], [19] but also the nucleation of other phases including primary phases such as the primary metastable $L1_2$-Al_3Zr phase often used to refine the grain size in Al alloys designed for 3D printing. Controlling the nucleation mechanism of the primary $L1_2$-Al_3X phase could be employed to optimize its nucleation efficiency with respect to the FCC Al grains. Further insights regarding this mechanism could be gained by conducting ab initio calculations such as the ones proposed in [38]–[40] to investigate the structure of binary Al-Zr undercooled liquids.

Acknowledgements

The authors are grateful to the AEROPRINT project supported by the Région Auvergne Rhône-Alpes. This work has benefited from the characterization equipment of the Grenoble INP - CMTC platform supported by the Centre of Excellence of Multifunctional Architectured Materials “CEMAM” n°ANR-10-LABX-44-01 funded by the Investments for the Future program. G. Renou is acknowledged for his technical support during the ACOM-TEM acquisitions. The authors would like to thank Dr. Alain Pasturel and Prof. Noel Jakse for fruitful discussions.

References

[1] S.A.M. Tofail, E.P. Koumoulos, A. Bandyopadhyay, S. Bose, L. O'Donoghue, C. Charitidis, Materials Today 21 (2018) 22–37.
[2] Q. Jia, P. Rometsch, S. Cao, K. Zhang, X. Wu, Materials & Design 174 (2019) 107775.
[3] R.A. Michi, A. Plotkowski, A. Shyam, R.R. Dehoff, S.S. Babu, International Materials Reviews 67 (2022) 298–345.
[4] H. Zhang, H. Zhu, X. Nie, J. Yin, Z. Hu, X. Zeng, Scripta Materialia 134 (2017) 6–10.
[5] Z. Fan, C. Li, H. Yang, Z. Liu, Journal of Materials Research and Technology 19 (2022) 194–207.
[6] R. Li, M. Wang, Z. Li, P. Cao, T. Yuan, H. Zhu, Acta Materialia 193 (2020) 83–98.
[7] A. Mehta, L. Zhou, T. Huynh, S. Park, H. Hyer, S. Song, Y. Bai, D.D. Imholte, N.E. Woolstenhulme, D.M. Wachs, Y. Sohn, Additive Manufacturing 41 (2021) 101966.
[8] B. Huang, Y. Liu, Z. Zhou, W. Cheng, X. Liu, Vacuum 200 (2022) 111030.
[9] R. Casati, M. Coduri, M. Riccio, A. Rizzi, M. Vedani, Journal of Alloys and Compounds 801 (2019) 243–253.
[10] S.Y. Zhou, Y. Su, H. Wang, J. Enz, T. Ebel, M. Yan, Additive Manufacturing 36 (2020) 101458.
[11] F. Leijon, S. Wachter, Z. Fu, C. Körner, S. Skjervold, J. Moverare, Materials & Design 211 (2021) 110129.
[12] A.B. Spierings, K. Dawson, M. Voegtlin, F. Palm, P.J. Uggowitzer, CIRP Annals 65 (2016) 213–216.
[13] J.R. Croteau, S. Griffiths, M.D. Rossell, C. Leinenbach, C. Kenel, V. Jansen, D.N. Seidman, D.C. Dunand, N.Q. Vo, Acta Materialia 153 (2018) 35–44.
[14] L. Li, R. Li, T. Yuan, C. Chen, M. Wang, J. Yuan, Q. Weng, Journal of Alloys and Compounds 821 (2020) 153520.
[15] A. Mehta, L. Zhou, T. Huynh, S. Park, H. Hyer, S. Song, Y. Bai, D.D. Imholte, N.E. Woolstenhulme, D.M. Wachs, Y. Sohn, Additive Manufacturing 41 (2021) 101966.
[16] R. Li, M. Wang, Z. Li, P. Cao, T. Yuan, H. Zhu, Acta Materialia 193 (2020) 83–98.
[17] Y. Wang, R. Li, T. Yuan, L. Zou, M. Wang, H. Yang, Materials Characterization 180 (2021) 111397.
[18] Q. Jia, P. Rometsch, P. Kürnsteiner, Q. Chao, A. Huang, M. Weyland, L. Bourgeois, X. Wu, Acta Materialia 171 (2019) 108–118.
[19] S. Griffiths, M.D. Rossell, J. Croteau, N.Q. Vo, D.C. Dunand, C. Leinenbach, Materials Characterization 143 (2018) 34–42.
[20] M. Opprecht, J.-P. Garandet, G. Roux, C. Flament, Acta Materialia 215 (2021) 117024.
[21] M. Opprecht, J.-P. Garandet, G. Roux, C. Flament, M. Soulier, Acta Materialia 197 (2020) 40–53.
[22] M. Rappaz, Ph. Jarry, G. Kurtuldu, J. Zollinger, Metall Mater Trans A 51 (2020) 2651–2664.
[23] G. Kurtuldu, P. Jarry, M. Rappaz, Acta Materialia 61 (2013) 7098–7108.
[24] J. Zollinger, B. Rouat, J. Guyon, S.K. Pillai, M. Rappaz, Metall Mater Trans A 50 (2019) 2279–2288.
[25] C. Galera-Rueda, M.L. Montero-Sistiaga, K. Vanmeensel, M. Godino-Martínez, J. Llorca, M.T. Pérez-Prado, Additive Manufacturing 44 (2021) 102053.
[26] M. Buttard, X. Bataillon, G. Renou, P. Lhuissier, J. Villanova, B. Chehab, P. Jarry, J.-J. Blandin, P. Donnadieu, G. Martin, Additive Manufacturing, Available online 23 November (2022) 103303
[27] I. Cazic, J. Zollinger, S. Mathieu, M. El Kandaoui, P. Plapper, B. Appolaire, Scripta Materialia 195 (2021) 113740.
[28] C. Galera-Rueda, X. Jin, J. LLorca, M.T. Pérez-Prado, Scripta Materialia 211 (2022) 114512.
[29] M. Buttard, B. Chehab, R. Shahani, F. Robaut, G. Renou, C. Tassin, E. Rauch, P. Donnadieu, A. Deschamps, J.-J. Blandin, G. Martin, Materialia 18 (2021) 101160.
[30] E.F. Rauch, J. Portillo, S. Nicolopoulos, D. Bultreys, S. Rouvimov, P. Moeck, Zeitschrift Für Kristallographie 225 (2010) 103–109.
[31] E.F. Rauch, P. Harrison, X. Zhou, M. Herbig, W. Ludwig, M. Véron, Symmetry 13 (2021) 1675.
[32] A. Valery, E. f. Rauch, L. Clément, F. Lorut, Journal of Microscopy 268 (2017) 208–218.

[33] X. Nie, H. Zhang, H. Zhu, Z. Hu, L. Ke, X. Zeng, Journal of Alloys and Compounds 764 (2018) 977–986.
[34] Z. Zhu, F.L. Ng, H.L. Seet, W. Lu, C.H. Liebscher, Z. Rao, D. Raabe, S. Mui Ling Nai, Materials Today 52 (2022) 90–101.
[35] X. Nie, H. Zhang, H. Zhu, Z. Hu, Y. Qi, X. Zeng, Materials Letters 248 (2019) 5–7.
[36] L. Zhou, H. Hyer, S. Park, H. Pan, Y. Bai, K.P. Rice, Y. Sohn, Additive Manufacturing 28 (2019) 485–496.
[37] F.C. Frank, J.S. Kasper, Acta Cryst 11 (1958) 184–190.
[38] A. Pasturel, N. Jakse, J. Chem. Phys. 146 (2017) 184502.
[39] N. Jakse, A. Pasturel, Phys. Rev. B 76 (2007) 024207.
[40] N. Jakse, A. Pasturel, J. Chem. Phys. 143 (2015) 084504.